Computers & Fluids 51 (2011) 85–99

Contents lists available at SciVerse ScienceDirect

Computers & Fluids

journal homepage: www.elsevier.com/locate/compfluid

Application of the method of manufactured solutions to the verification of a pressure-based finite-volume numerical scheme

João Marcelo Vedovoto [a,*], Aristeu da Silveira Neto [a], Arnaud Mura [b], Luis Fernando Figueira da Silva [c]

[a] Faculty of Mechanical Engineering, Federal University of Uberlândia, Uberlândia, MG 38400-902, Brazil
[b] Institut Pprime, UPR3346 CNRS, ENSMA, BP40109, 86961 Poitiers, France
[c] Pontifícia Universidade Católica do Rio de Janeiro, Department of Mechanical Engineering, Rio de Janeiro, RJ 22453-900, Brazil

ARTICLE INFO

Article history:
Received 10 March 2010
Received in revised form 29 April 2011
Accepted 29 July 2011
Available online 18 August 2011

Keywords:
Code verification
Methods of manufactured solutions
Low Mach number approximation
Pressure based solver
Variable density flows
Combustion

ABSTRACT

The present study reports a numerical procedure based on a series of tests that make use of the method of manufactured solutions (MMS) and allow to evaluate the effective numerical performance with respect to the theoretical order of accuracy. The method is applied to a pressure-based finite volume numerical scheme suited to variable density flows representative of those encountered in combustion applications. The algorithm is based on a predictor–corrector time integration scheme that employs a projection method for the momentum equations. A physically consistent constraint is retained to ensure that the velocity field is solved correctly. The MMS application shows that the combination of this velocity constraint and the variable-coefficient Poisson solver is of fundamental importance to ensure both the numerical stability and the expected order of accuracy. Especially, the resort to an inner iteration procedure gives rise to undeniable improvements in terms of both the order of accuracy and error magnitude. The MMS applications confirm the interest of the method to conduct a preliminary check of the performance of any numerical algorithm applied to both fully incompressible and variable density flows. Finally, the analysis is ended by the application of the retained pressure-based finite-volume scheme to the numerical simulation of mixing layers featuring increasing values of the density contrast. The corresponding results shed some light onto the stability and robustness of the numerical scheme, important issues that are not addressed through MMS analyses.

1. Introduction

Low Mach number variable density flows arise in several natural as well as technological processes, including meteorological flows or combustion in energy conversion devices (engine, turbojets, etc.). Regarding the prediction and understanding of such a category of flows, the extensive use of mathematical and numerical techniques is unavoidable. Hence, as the mathematical and numerical methods become more complex, the procedures of validation and verification of computer codes must evolve as well. The present work aims at systematically demonstrating the procedure of verification of a CFD code designed to perform the numerical simulation of low Mach number flows. Although such a procedure appears as a necessary preliminary step before tackling the computational modeling of turbulent combustion problems of interest to the authors [1–4], the literature still lacks detailed information regarding the subject, especially concerning the verification of variable density low Mach number flows. In order to clarify the differences between the words verification and validation, we used the following definitions. Verification aims at providing information on whether the mathematical model has been well implemented according to initial design or not, whereas validation refers to how closely the correctly implemented mathematical model mimics a given set of experimental data [5]. The solutions of the balance equations (mass, momentum, energy, species mass fractions, etc.) are deemed sufficient to represent any flows irrespective of their characteristic velocity, provided that the continuum hypothesis holds, and once suitable constitutive equations for the fluids of interest are provided. However, when dealing with discrete approaches for solving such a system of balance equations, the numerical techniques do involve, invariably, errors. These errors have different sources, spanning from unavoidable roundoff errors to mere programming mistakes (bugs), hence emphasizing the crucial need for well defined procedures to evaluate the numerical accuracy [6]. Moreover, it is of fundamental importance to be able to characterize the capabilities of a numerical approach, i.e., it is imperative to determine whether (or not) the retained mathematical/numerical scheme is suitable to cope with the problem of interest.

The manuscript is organized as follows: before introducing the method of manufactured solutions (MMS) that is retained here to proceed with the verification of low Mach number schemes, we

* Corresponding author.
E-mail address: jmvedovoto@mecanica.ufu.br (J.M. Vedovoto).

0045-7930/$ - see front matter © 2011 Elsevier Ltd. All rights reserved.
doi:10.1016/j.compfluid.2011.07.014

first briefly review the existing strategies used to perform such numerical simulations. Further, we present the specificities of the computational model adopted herein, and then focus on the MMS procedure retained for the verification. Finally, the analysis is completed by the application of the retained pressure-based finite-volume scheme to the numerical simulation of mixing layers featuring increasing values of the density contrast, a critical parameter for such a kind of numerical schemes.

1.1. Low Mach number limit

In the present work, we are interested in low velocity flows, i.e., in the incompressible regime, but featuring non negligible density variations, the so-called low Mach number flows. There are basically two broad classes of numerical methodologies to deal with this kind of flows: those relying on density-based solvers, i.e., based on methods usually retained for compressible flows [7], and those relying on pressure-based solvers, such as those retained to perform the numerical simulation of incompressible flows.

The density-based methods represent a wide class of numerical schemes originally developed to study compressible flows [8]. Turkel et al. [9] determined that the set of discretized equations retained for the numerical simulation of a compressible flows fails to provide an accurate solution for an incompressible flow. The simulations of incompressible flows based on the fully compressible method, with no modifications to reduce the disparity existing between the flow velocity and the speed of sound, are found impracticable due to the associated computational costs. In this case, temporal integration schemes, whatever they are explicit or implicit, are penalized. In the former case, the Courant–Friedrichs–Lewy (CFL) condition, that must be satisfied at each time step to enforce the numerical stability of the numerical integration scheme, leads to prohibitively small time step values due to the prevailing influence of acoustic waves propagation. In the case of implicit methods such a disparity induces large differences in the characteristic eigenvalues of the algebraic system to be solved, which becomes ill-conditioned, leading therefore to extremely high-cost iterative solutions [10]. Two distinct sets of techniques have been proposed to achieve better convergence properties of density-based solvers, in the limit of low Mach number flows: preconditioning and perturbation methods. Both techniques strive to minimize the stiffness of the algebraic system that results from the discretization of the balance equations. The first technique pre-multiplies the temporal derivatives by a preconditioning matrix, whose choice is determined according to the problem to be analyzed [11], thus leading to a new set of equations. As a consequence, the initial (stiff) system is altered. The approach essentially aims at re-scaling the characteristic eigenvalues with respect to the original system, so that eigenvalues of similar orders of magnitude can be obtained, thus leading to a better conditioned system [9,12,13]. The second set of techniques is the perturbation methods, or asymptotic analysis. In this case, a perturbed form of the equations is used to reduce the stiffness of the algebraic system of equations. A Taylor expansion is performed in terms of the Mach number decoupling the acoustic waves from the equations, and replacing them with a set of pseudo-acoustic forms, where the wave velocities become the same order of magnitude as the fluid velocity. Such a procedure alters the velocity of the acoustic waves in order to allow the numerical integration to be performed with larger time steps [10,11]. Other methodologies have been also developed for the purpose of considering density variations, such as the artificial compressibility methods [14,15], and the Pressure Gradient Scaling approach [16–19].

In contrast to the methodologies discussed above, pressure-based methods have been initially proposed to solve fully incompressible flows, retaining the pressure as one of the primary variables. Such numerical schemes that are often referred to as pressure-corrections methods, or projection methods, evaluate the pressure and velocity fields in a segregated manner [20,21]. In pressure-based methods, the pressure does not play a thermodynamic role, but ensures the incompressibility condition, which leads to a discretization scheme based on a separation of operators (splitting method). In a first step, momentum equations are solved to obtain an estimated velocity field, based on a previous evaluation of pressure. The velocity field should be solenoidal, and this property is enforced by a subsequent projection step within the subspace of divergence-free vectorial fields. Such projection, which defines the corrector step, relies on the Hodge decomposition theorem [22]. The pioneering works in this field [20,23] have provided the basis for the development of several projection schemes that are still currently used.

As previously mentioned, in the low Mach number regime, the compressibility effects have a negligible influence on the momentum transport and the pressure is only a weak function of density. To prevent significant inaccuracies when performing the evaluation of pressure, it is usually divided into two distinct components:

$$P(\mathbf{x},t) = P_o(t) + P'(\mathbf{x},t), \tag{1}$$

where P_o is a reference pressure level,[1] with $P_o(t)/P_o = O(1)$, and $P(\mathbf{x},t)/P_o = O(Ma^2)$. It is worth noting that $P_o(t)$ is often referred to as the thermodynamic pressure, whereas $P'(\mathbf{x},t)$ is called the dynamic pressure since it is directly related to modifications of the velocity field.

Using such a decomposition, the thermodynamic pressure appears in the equations of state and energy conservation only, vanishing in the momentum equation. Since its gradient is zero everywhere, only the gradient of the dynamic pressure component remains. It is worth noting that this procedure significantly accelerates the convergence only if the pressure fluctuations remain sufficiently small. A wide class of methods used to perform the numerical simulations of low Mach number flows, is based on such a predictor–corrector methods. Several works [24–31] share such pressure–velocity coupling. For further details, the interested reader is referred to the analysis of Rider et al. [32] where an extensive discussion about robust projection methods applied to variable density low Mach number flows has been reported.

In the present work, the method of manufactured solutions is used to assess the capability of a CFD solver that has been recently extended to the consideration of variable density flows. The retained numerical approach falls into the second category discussed above, i.e. the one associated with pressure-based formulations. The details of corresponding numerical strategy will be described later on. We now enter into the core of the present study and introduce the method of manufactured solutions.

1.2. Code verification and manufactured solutions

The resort to the method of manufactured solutions is progressively becoming a classical, and well accepted methodology retained in the framework of numerical code verification [33]. There is an undeniable interest in the use of such a method to quantify accurately numerical capabilities before using computational programs to perform the simulation of complicated physical systems. Herein the method is applied to a low Mach number flow solver. To represent the corresponding variable density flows, we consider a mathematical model in which the primary transported variables are the density $\rho(\mathbf{x},t)$, the three velocity components $u_i(\mathbf{x},t)$ $(i = 1,2,3)$, and the temperature.

[1] Since we are interested in high Froude number gaseous flows, the effects of gravity are not considered, hence $P_o(t)$ is a function of the time only.

The non-dimensional balance equations for the cited variables in space, (x_i, $i = 1,2,3$), and time, t, are summarized below along with an equation of state that relates the thermodynamic component of the pressure to density and temperature. It is worth noting that dimensional quantities are now referred to with the superscript '$\wedge$'.

$$\frac{\partial \rho}{\partial t} + \frac{\partial \rho u_i}{\partial x_i} = S_\rho, \tag{2}$$

$$\frac{\partial \rho u_i}{\partial t} + \frac{\partial \rho u_i u_j}{\partial x_j} = -\frac{\partial P}{\partial x_i} + \frac{1}{Re}\frac{\partial}{\partial x_j}\tau_{ij} + S_{u_i}, \tag{3}$$

$$\tau_{ij} = -\frac{2}{3}\mu\frac{\partial u_k}{\partial x_k}\delta_{ij} + \mu\left(\frac{\partial u_i}{\partial x_j} + \frac{\partial u_j}{\partial x_i}\right), \tag{4}$$

$$P = P_o(t) + P'(\mathbf{x}, t); \quad P_o = \rho\phi. \tag{5}$$

The above set of equations is obtained in a non-dimensional form using:

$$x_i = \hat{x}_i/L_{ref}, \quad t = \hat{t}u_{ref}/L_{ref}, \quad u_i = \hat{u}_i/u_{ref}, \tag{6}$$

$$P = \frac{\widehat{P}}{(\rho_{ref}u_{ref}^2)}, \quad \rho = \hat{\rho}/\rho_{ref}. \tag{7}$$

In Eq. (5), $P_o(t)$ is the thermodynamic pressure, a function of time only, $P'(\mathbf{x},t)$ is the dynamic pressure, henceforth denoted only by p. In the same equation, the variable ϕ stands for a reduced temperature, defined by

$$\phi = (T - T_u)/(T_b - T_u), \tag{8}$$

where T_b (resp. T_u) denotes the maximal (resp. minimal) value of the temperature, in such a manner that $\phi \in [0;1]$. For instance, if we consider a premixed flame propagating towards unburned reactants, T_u and T_b stand for the temperature in the fresh mixture and fully burned products of combustion respectively. The transport equation for the reduced temperature writes:

$$\rho C_p\frac{\partial \phi}{\partial t} + \rho C_p u_i\frac{\partial \phi}{\partial x_i} = \frac{1}{RePr}\frac{\partial}{\partial x_j}\left(\kappa\frac{\partial \phi}{\partial x_j}\right) + \left(\frac{\gamma - 1}{\gamma}\right)\frac{dP_o}{dt} + S_\phi, \tag{9}$$

where $Pr = \mu_{ref}C_{p_{ref}}/\kappa_{ref}$, and $Re = \rho_{ref}u_{ref}L_{ref}/\mu_{ref}$, denote the Prandtl and Reynolds numbers.

It is noteworthy that, in the previous set of conservation equations (Eqs. (2), (3), and (9)), temperature dependent variables, such as the transport properties: viscosity μ, and thermal conductivity κ, and the heat capacity C_p, have been made non dimensional with respect to their values at temperature T_u. The corresponding values are denoted μ_{ref}, κ_{ref}, and $C_{p_{ref}}$. Finally, the source terms S_{u_i}, S_ρ, and S_ϕ have been included in Eqs. (2), (3), and (9), just for the sake of generality.

The method of manufactured solutions (MMS) consists in developing *a priori* known analytical solutions of the system of governing equations. The pioneering works that make use of manufactured solutions with the objective of verifying the order of accuracy of a given numerical code can be assigned to Steinberg and Roache [33], Roache et al. [34] and Roache [35]. These manufactured solutions modify the original equations by adding a 'source term' into their right hand side, such as those presented above in Eqs. (2), (3) and (9). To construct the manufactured solution a set of almost arbitrary functions are selected and substituted into the considered system PDEs, thus allowing to solve its derivatives analytically. The result of such a substitution is the ' source term' mentioned above. The source term is then considered as an input to the numerical code, in such a manner that it becomes able to reproduce the manufactured solution. Salari and Knupp [36] provide a well documented guideline for creating manufactured solutions as well as the procedure for obtaining the corresponding source terms and further analysis of the results.

In order to obtain the order of accuracy of the developed numerical implementation, a quantitative metric of the error is chosen, and successive grid refinements are performed. As the error metric decays with the grid refinement, it is evaluated as a function of the characteristic mesh size h.

The method appears as very appealing but it should be noted that the arbitrary nature of the analytical functions must satisfy, at least, the following conditions:

- They must be continuous smooth function of independent variables (problems involving discontinuities are generally dealt with using lower order algorithms due to stability issues).
- The solution must be continuously differentiable up to the order required by the corresponding terms in the governing equations.
- To avoid numerical difficulties, manufactured solutions should avoid negative values for quantities that are physically defined as positive semi-definite (e.g. density, molecular viscosity).
- If periodic boundary conditions are chosen, the solution must be periodic as well to avoid the development of discontinuities.

For a given level of resolution, we define $\Phi^h_{(i,j,k)}$ as the discrete value of any variable Φ of interest, e.g. the density, velocity components, pressure or reduced temperature, at any point (i,j,k), and $\Phi^e_{(i,j,k)}$ the corresponding value of the manufactured solution. The first step of the verification procedure now requires to define a metric of the numerical error, denoted Ψ_h in the following, in order to quantify subsequently the error decay rate obtained for decreasing values of the characteristic grid mesh size h.

Retaining the L_2-norm as a relevant metric of the numerical error, we introduce:

$$\Psi_h = L_2\left(\Phi^h_{(i,j,k)}\right) = \sqrt{\frac{1}{N}\sum\nolimits_{i,j,k}\left(\Phi^h_{(i,j,k)} - \Phi^e_{(i,j,k)}\right)^2}, \tag{10}$$

where N denotes the total number of grid points.

The ratio of error decay is defined according to:

$$r_e = \log\left(\frac{\Psi_{2h}}{\Psi_h}\right), \tag{11}$$

with Ψ_{2h} the numerical value of the metric error obtained on a grid with a characteristic mesh size $2h$.

Following the nomenclature retained in [36], we define also the order of accuracy q as:

$$q \approx \frac{r_e}{log(2)}. \tag{12}$$

Using Eq. (12), it is possible to verify that the characteristic error decay ratio, using grids with characteristics mesh sizes $2h$ and h, for methods of order of accuracy $q = 1$, 2 and 3, must be, approximately, 2, 4 and 8, respectively. It is worth noting that, although possible, the value of r_e does not always converge monotonically as the mesh is progressively refined, and it may exhibit some oscillations.

Directly related to the results obtained from the application of the MMS procedures are the characteristics of the computational solver under consideration and especially the associated orders of accuracy of the retained numerical schemes. The next section therefore aims at providing all the necessary information about the solution procedure on which the MMS procedures will be subsequently applied.

2. Description of the retained numerical scheme

The discretization of the set of Eqs. (2), (3) and (9) is now presented. In transient flows the integration in time requires the choice of a suitable time marching scheme. Temporal integration

schemes are essentially controlled by the Courant criterion $Co = (u_i \delta t)/\delta x_i$, $i = 1,2,3$. Explicit schemes exhibit numerical stability issues when using Courant number values larger than unity. However, such a numerical limitation does not apply to implicit or semi-implicit discretizations. Ferziger and Peric [14] provide an introduction to several types of classical temporal integration methods. Examples of semi-implicit approaches can be found in [37], and a detailed evaluation of various semi-implicit schemes has been reported in [38]. The temporal integration schemes retained in the present work are fully implicit, in such a manner that it is possible to reach statistically steady regimes faster than by resorting to explicit time integration techniques.

Arscher et al. [38] proposed a semi-discretized arrangement in such a way that any differential equation could be temporally integrated using second order semi-implicit schemes:

$$\frac{1}{\Delta t}\left[\left(\gamma+\frac{1}{2}\right)u^{n+1}-2\gamma u^{n}+\left(\gamma-\frac{1}{2}\right)u^{n-1}\right]=(\gamma+1)\zeta(u^{n})-\gamma\zeta(u^{n-1}) + \left[\left(\gamma+\frac{c}{2}\right)\epsilon(u^{n+1})+(1-\gamma-c)\epsilon(u^{n})+\frac{c}{2}\epsilon(u^{n-1})\right], \tag{13}$$

where $\zeta(u)$ and $\epsilon(u)$ stand for, respectively, diffusive and advective contributions to the differential equation, and n represents the time level. Depending on the values retained for constants γ and c, different time integration schemes can be obtained [38]:

- Crank–Nicolson Adams–Bashfort (CNAB): $(\gamma, c) = (0.5, 0.0)$.
- Modified Crank–Nicolson Adams–Bashfort (MCNAB): $(\gamma, c) = (0.5, 0.125)$.
- Crank–Nicolson Leap Frog (CNLF): $(\gamma, c) = (0.0, 1.0)$.
- Semi-Backward Difference Formula (SBDF): $(\gamma, c) = (1.0, 0.0)$.

In the present work, instead of a semi-implicit, a fully implicit scheme is adopted. However, the organization allowed by Eq. (13) remains very attractive, since it includes the possibility of (i) describing several methods of temporal discretization and, hence, (ii) choosing the more adequate for a given problem. Retaining the same values of the constants γ and c, Eq. (13) can be adapted within a fully implicit framework as follows:

$$\frac{1}{\Delta t}\left[\left(\gamma+\frac{1}{2}\right)u^{n+1}-2\gamma u^{n}+\left(\gamma-\frac{1}{2}\right)u^{n-1}\right]=\left(\gamma+\frac{c}{2}\right)\left(\zeta(u^{n+1}) + \epsilon(u^{n+1})\right)+(1-\gamma-c)\left(\zeta(u^{n})+\epsilon(u^{n})\right)+\frac{c}{2}\left(\zeta(u^{n-1})+\epsilon(u^{n-1})\right). \tag{14}$$

Applying Eq. (3) in Eq. (14), and re-arranging the different terms, the momentum equation, once discretized in time takes the following form:

$$\frac{(\gamma+0.5)\rho^{n+1}u_i^{n+1}-(2\gamma)\rho^{n}u_i^{n}+(\gamma-0.5)\rho^{n-1}u_i^{n-1}}{\Delta t} = -\frac{\partial p^{n+1}}{\partial x_i}+(\gamma+0.5c)m_2+(1-\gamma-c)m_1+(0.5c)m_0+S_{ui}^{n+1}, \tag{15}$$

where we defined:

$$m_{k+1}=\left(\frac{\partial \tau_{ij}^{n+k}}{\partial x_j}-\frac{\partial \rho^{n+k}u_i^{n+k}u_j^{n+k}}{\partial x_j}\right), \quad k=-1,0,1. \tag{16}$$

As mentioned previously, the choice of the constant values γ and c, allows to recover the Crank–Nicolson method $(\gamma, c) = (0.5, 0.0)$, the Modified Crank–Nicolson $(\gamma, c) = (0.5, 0.125)$, the Leap Frog method $(\gamma, c) = (0.0, 1.0)$ and, the Backward Difference Formula – BDF, $(\gamma, c) = (1.0, 0.0)$.

Finally, it is wort recalling that, that through Eq. (15), the fully implicity framework retained here requires the numerical resolution of a large algebraic system.

Since a fully implicit fractional step method is used in the present work, a Poisson type equation must be solved to apply a pressure correction to both velocity and pressure fields. To provide such an equation, we write Eq. (15), with the pressure derivative evaluated at time level n:

$$\frac{(\gamma+0.5)\rho^{n+1}\tilde{u}_i^{n+1}-(2\gamma)\rho^{n}u_i^{n}+(\gamma-0.5)\rho^{n-1}u_i^{n-1}}{\Delta t} = -\frac{\partial p^{n}}{\partial x_i} + (\gamma+0.5c)m_2+(1-\gamma-c)m_1+(0.5c)m_0+S_{ui}^{n+1}, \tag{17}$$

where $\tilde{u}_i^{n+1}$ stands for the estimated velocity field. Subtracting Eq. (17) from Eq. (15), defining $Q = p^{n+1} - p^{n}$, and rearranging the different terms, one obtains:

$$\frac{\rho^{n+1}(\gamma+0.5)}{\Delta t}\left(\tilde{u}_i^{n+1}-u_i^{n+1}\right)=\frac{\partial Q}{\partial x_i}, \tag{18}$$

we then proceed classically by taking the divergence of Eq. (18):

$$\frac{(\gamma+0.5)}{\Delta t}\left(\frac{\partial \tilde{u}_i^{n+1}}{\partial x_i}-\frac{\partial u_i^{n+1}}{\partial x_i}\right)=\frac{\partial}{\partial x_i}\left(\frac{1}{\rho^{n+1}}\frac{\partial Q}{\partial x_i}\right). \tag{19}$$

In situations where the density can be considered to be constant, at least along a streamline, the second derivative at the LHS of Eq. (19) is zero due the incompressibility condition. However, when density variations arise from temperature (and potential composition) variations as encountered for instance in reactive flows, such term can no longer be discarded.

In the low Mach number flows under consideration, the density is solely determined by the temperature and thermodynamic pressure fields. The energy equation plays the role of an additional constraint on the velocity field, which is enforced by the dynamic pressure. This constraint acts onto the flow field divergence, and it is related to the total derivative of the density field, which involves – through the equation of state Eq. (5) – the total derivatives of both pressure and temperature. The latter can be expressed thanks to the energy conservation equation, i.e. Eq. (9), thus leading to:

$$\frac{\partial u_i}{\partial x_i}+S_c=\frac{1}{C_pP_o}\left\{\frac{1}{RePr}\frac{\partial}{\partial x_i}\left(\kappa\frac{\partial \phi}{\partial x_i}\right)+\left(\frac{\gamma-1}{\gamma}-C_p\right)\frac{dP_o}{dt}+S_\phi+C_pTS_\rho\right\}, \tag{20}$$

where S_c is a mathematical source term associated with the constraint itself. This source term, which is added to the constraint, will be used in the subsequent application of the method of manufactured solutions devoted to the low Mach number scheme verification. The equation for pressure correction, for low Mach number flows simulations may therefore be written as:

$$\frac{\partial}{\partial x_i}\left(\frac{1}{\rho^{n+1}}\frac{\partial Q}{\partial x_i}\right)=\frac{(\gamma+0.5)}{\Delta t}\left\{\frac{\partial \tilde{u}_i^{n+1}}{\partial x_i}-\frac{1}{C_pP_o}\left[\frac{1}{RePr}\frac{\partial}{\partial x_i}\left(\kappa\frac{\partial \phi}{\partial x_i}\right)\right]\right\} + \frac{(\gamma+0.5)}{\Delta t}\left[\left(\frac{\gamma-1}{\gamma}-C_p\right)\frac{dP_o}{dt}+S_\phi+C_pTS_\rho-S_c\right]. \tag{21}$$

Once the pressure correction is evaluated, the velocity field can be updated:

$$u_i^{n+1}=\tilde{u}_i^{n+1}-\left(\frac{\Delta t}{(\gamma+0.5)\rho^{n+1}}\right)\frac{\partial Q}{\partial x_i}. \tag{22}$$

The constraint given by Eq. (20) in variable density flows has been previously discussed, for instance, in [29,39]. Moreover, an inner iterative process can be used to enhance both stability and convergence of the solution process. Further comments about such a procedure and its effects on the numerical convergence are deferred to the section devoted to the validation of low Mach number manufactured solutions. Finally, it is worth recalling that, for incompressible flows simulations, the constraint presented above is no longer necessary.

Important factors that directly impact the performance of a numerical method that seeks to solve variable density incompressible flows are: (i) the choice of the variables arrangement in the computational grid, (ii) the type and order of accuracy of the numerical scheme retained to perform the discretization in space of both viscous and advective terms, and (iii) the type and order of accuracy of the method chosen to perform the temporal integration.

If the discretization relies on a finite-volume (FV) approach, it is necessary to evaluate vectorial fields coupled to scalar fields, as it is the case when the Navier–Stokes equations are considered. The issue associated to the positioning of the primary variables in the computational grid must be carefully accounted. Several options exist, but they may be classified into two principal groups: staggered or co-located grids. In the former case, the vectorial and scalar variables are positioned in different locations. In the latter, all physical variables are evaluated at the same location. This is the simplest choice for implementation, in particular when distributed computing strategies are to be applied. However, in incompressible flows, if the velocity and pressure are positioned in the same location, decoupling instabilities, often referred to as checkerboard patterns can arise [7,14,28].

The discretization procedure retained for the momentum equation is basically identical for both the staggered and the co-located arrangements. Nevertheless, with the latter, the velocity components, positioned at the center of the control volumes must be interpolated to their faces. The most common procedure is to use the Rhie–Chow interpolation [40]. Shen et al. [41] underline that the Rhie–Chow interpolation produces excellent results when steady-state solutions are sought for, and large time steps used, but pressure field oscillations may arise for small time steps and during transient simulations. Versteeg and Malalasekera [42], and Ferziger and Peric [14], argue that there is no intrinsic physical requirement that all variables share the same location. For Cartesian grids, the concept of staggered grid was introduced in Ref. [43]. If second order of accuracy schemes are retained for spatial discretization, such an arrangement does not require additional interpolations, which otherwise would be necessary for a co-located grid. Finally, the major advantages of the staggered variable arrangement is that the pressure terms are naturally discretized by second order accuracy central differences scheme, without resorting to interpolation rules, and the evaluation of mass fluxes at the faces of control volumes is straightforward, which leads to a strong coupling between pressure and velocity, thus avoiding spurious instabilities in the calculated pressure field.

The numerical method chosen for solving the variable density momentum, reduced temperature and Poisson equations is based on a three-dimensional, conservative, staggered, finite-volume discretization. The central difference scheme (CDS) is applied to express both diffusive and advective contributions of the present finite-volume scheme. Depending on the class of flows simulated, iterative solvers may fail to converge when applied to the algebraic equation systems derived from central difference approximations of convective fluxes. The main reason is associated to odd–even decoupling and, hence, the corresponding oscillations should be removed to avoid numerical instabilities. Practically, the elimination of these spurious short waves is obtained by introducing artificial dissipation through additional damping terms in the equations [44] or, more efficiently, through filtering procedures [45] without affecting the physical long waves. It is also possible to apply a deferred correction approach on the advective terms of the balance equations, such approach, designed to improve stability, is described for instance in [14]. In this respect, it seems worth noting that the last solution, i.e., the use of the deferred correction approach, was successfully tested against the manufactured solutions described herein. The corresponding detailed results are not reported herein only for the sake of conciseness.

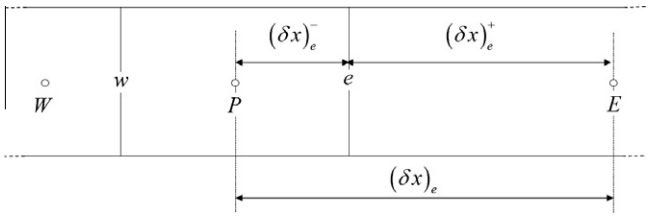

Fig. 1. Non-uniform finite-volume grid and distances associated to the face *e*.

A fully implicit approach is adopted, and the resulting linear systems are solved using the MSIP – Modified Strongly Implicit Procedure [46]. The numerical code developed is capable of performing massively parallel distributed computations also. The corresponding parallelization strategy relies on a three-dimensional Cartesian topology of domain decomposition, its detailed description is outside the scope of the present study.

The structure adopted for the computational grid, can be non-uniform in such a manner that it is necessary to perform interpolations to discretize any spatial derivatives. Such interpolations are obtained by using classical distance-weighted rules [14] e.g., to determine the value of a scalar property, θ, on a face *e*, the following expression is used: $\theta_e = \theta_E \Lambda_e + \theta_P(1 - \Lambda_e)$, where:

$$\Lambda_e = \frac{(\delta x)_e^-}{(\delta x)_e}. \tag{23}$$

The indexes *P*, *E* and *e*, are, respectively, the center of the current control volume, the center of the left control volume, and the position of the face of the control volume centered in *P*, that lies between *P* and *E*, as can be seen in Fig. 1.

The iterative procedure, for each time step, is summarized in Table 1:

It is important to underline that the algorithm described above ensures mass conservation within each single iteration step. Increasing the number of inner iterations improves both its precision and numerical stability, as will be shown in the following section that is devoted to the verification of the numerical algorithm just described.

Table 1
Algorithm 1 – Projection method with inner iteration procedure.

[1]	The scalar equation for reduced temperature [Eq. (9)] is advanced in time using the Crank–Nicolson integration scheme, [Eqs. (15), (16)] with $(\gamma, c) = (0.5, 0.0)$
[2]	The equation of state [Eq. (5)] is evaluated, yielding the density in the actual time step
[3]	The momentum equations [Eq. (17)] are advanced in time, yielding the estimated velocity field $\bar{u}_i^{n+1}$
[4]	The variable-coefficient Poisson equation [Eq. (21)] is solved yielding the pressure correction *Q*, the pressure and velocity fields are updated [Eq. (22)]
[5]	The continuity equation [Eq. (2)] is evaluated to check the mass conservation
[6]	Returns to item [1], until the cycling process is finished
[7]	Time is advanced: $t^{n+1} = t^n + \delta t^n$
[8]	Process is repeated from step [1] until $t^{n+1} = t_{end}$

3. Applications of the method of manufactured solutions

We provide now the detailed guidelines for verification and cross-checks of low Mach number codes through the application of the method of manufactured solutions. The process of verification presented herein is divided into two distinct parts. First, the numerical code is tested using a manufactured solution that aims at verifying the order of accuracy for an incompressible solution (zero Mach number limit). This is performed using solutions based on sine and cosine functions, built in such a manner that the velocity divergence is zero. A second set of tests aims at mimicking the propagation of a corrugated flame front that separates heavy from light gases. The application of the method of manufactured solutions still remains more scarce for such low Mach number situations. If we except the expression of the equation of state, the solution retained to perform this analysis is the same as the one previously considered in the recent studies conducted by Shunn and Ham [47], and Shunn and Knupp [48]. This second set of tests clearly aims at evaluating the numerical capabilities of the developed code to deal with variable density flows as those encountered in combustion problems of interest to the authors.

3.1. Verification of an incompressible solution

Following the recent work conducted by [49 and 50], the set of functions reported below is retained as a possible solution for velocity, pressure and scalar fields in the limit of a zero Mach number scheme:

$$u_e = \sin^2(2\pi x + 2\pi y + 2\pi z + t), \tag{24}$$

$$v_e = \cos^2(2\pi x + 2\pi y + 2\pi z + t), \tag{25}$$

$$w_e = 1, \tag{26}$$

$$p_e = \cos(2\pi x + 2\pi y + 2\pi z + t), \tag{27}$$

$$\phi_e = K_{\phi_1} + \frac{1}{K_{\phi_2}} + \cos(2\pi x + 2\pi y + 2\pi z + t). \tag{28}$$

In the previous equations K_{ϕ_1} and K_{ϕ_2} are constant parameters, t is the time. The subscript e stands for the manufactured solutions of the primary variables, i.e. the three velocity components, pressure and reduced temperature.

The computational domain retained for the present numerical simulations is a cube of dimensions $[0,1]\times[0,1]\times[0,1]$, in x, y and z directions respectively. The time step is set constant and equal to 10^{-4}. The parameters K_{ϕ_1} and K_{ϕ_2} are fixed respectively to 1 and 0.5. The constant values of density and viscosity are set to unity. The variable coefficient Poisson solver is used, however, no constraint is enforced for such incompressible solution. Table 2 reports the grid refinement, the decay of L_2 norm and the resulting order of accuracy q.

The results gathered in Table 2 are illustrated in Fig. 2. For the incompressible solution, the numerical code is shown to yield at least second order of accuracy for velocity. For the scalar variable ϕ, second order of accuracy is achieved as well, although minor oscillations arise. Finally, concerning the pressure, it is possible to note a continuous increase of the order of accuracy as the computational mesh is refined, however, its value does not exceed 1.89.

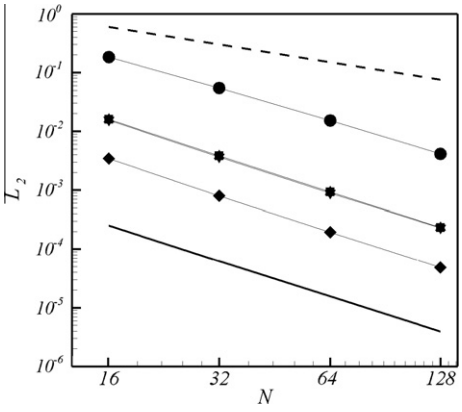

Fig. 2. L_2 norm of the Zero Mach Number manufactured solution. ■: u, ▲: v, ♦: w, ▼: ϕ, •: p. The solid line stands for the second order decay, and the dashed line stands for first order decay.

Such an analysis of the incompressible solution under consideration clearly demonstrates that, in terms of numerical accuracy, the numerical code we developed is a good candidate to perform Large Eddy Simulations of constant density turbulent flows that requires at least second order accuracy.

The preliminary key step associated with the verification of the numerical code being performed for an incompressible regime, we now turn to variable density flows.

3.2. Verification of the low-Mach number solution

The set of manufactured solutions retained in the present section are similar to those introduced in the previous studies by Shunn and Knupp [48] and Shunn and Ham [47]. However, it is used here with a different equation of state, which involves a different pressure–velocity coupling. It is also worth mentioning that we are interested in density ratio variations representative of those encountered in flames, which are significantly smaller than those reported in [47].

The manufactured solutions are not necessarily related to an expected physical solution, however, a solution that attempts to represent some relevant features of a given problem becomes not only a tool to assess the order of accuracy, but also provides a pertaining preview of the behavior of the numerical code, when applied to situations of interest. In this sense, the set of analytical functions reported below gathers some interesting features of a propagative combustion front.

$$\phi_e = \frac{1+\tanh[b\hat{x}\exp(-\omega t)]}{\left(1+\frac{\rho_0}{\rho_1}\right)+\left(1-\frac{\rho_0}{\rho_1}\right)\tanh[b\hat{x}\exp(-\omega t)]}, \tag{29}$$

$$\rho_e = \frac{P_o}{\phi_e}, \tag{30}$$

$$u_e = \frac{\rho_1-\rho_0}{\rho_e}\left\{-\omega\hat{x} + \frac{\omega\hat{x}-u_f}{\exp[2b\hat{x}\exp(-\omega t)]+1} + \frac{\omega\log[\exp(2b\hat{x}\exp(-\omega t))+1]}{2b\exp(-\omega t)}\right\}, \tag{31}$$

$$v_e = v_f, \tag{32}$$

$$w_e = 0, \tag{33}$$

$$p_e = 0, \tag{34}$$

Table 2
Order of accuracy for Dirichlet boundary conditions and constant physical properties.

Domain	16^3	q	32^3	q	64^3	q	128^3	q
L_2u	1.60E−02	–	3.80E−03	2.07	9.30E−04	2.03	2.33E−04	2.00
L_2v	1.60E−02	–	3.80E−03	2.07	9.30E−04	2.03	2.33E−04	2.00
L_2w	3.42E−03	–	7.98E−04	2.10	1.94E−04	2.04	4.86E−05	2.00
L_2p	1.82E−01	–	5.44E−02	1.74	1.52E−02	1.84	4.10E−03	1.89
$L_2\phi$	1.54E−02	–	4.10E−03	2.08	8.88E−04	2.03	2.29E−04	1.96

where $\hat{x} = u_f t - x + a\cos[k_2(v_f t - y)]$ and a, b, k_2, ω, u_f, v_f and P_o are constant parameters.

It is important to point out that the manufactured solution must be compatible with the full set of equations that governs the evolution of the system under consideration, and this also includes the equation of state and the resulting constraint that applies to the velocity field through Eq. (20). The above manufactured solution does not fulfill, by itself, such a requirement, and the source term S_c, previously introduced in Eqs. (20) and (21), must be now considered. Its expression, which is a rather cumbersome combination of exponential and hyperbolic functions, is not reported here but included as a supplementary material for readers who are interested to perform the evaluation of their own codes. The corresponding source term is evaluated in the same manner as S_{u_i} and S_ϕ, i.e. the exact functions (Eqs. (29)–(34)) are substituted in Eq. (20), and, after solving the derivatives analytically, one obtains the expression of S_c. Eqs. (29)–(34) satisfy the mass balance equation with $S_\rho = 0$, however, non-zero source terms also appear in momentum, (S_{u_i}), and reduced temperature transport equation (S_ϕ).

Fig. 3 displays the temporal evolution of the density field. It is possible to note that, as the time passes, the front is simultaneously advected and diffused. The computational domain is a box of $[-1,2]\times[-0.5,0.5]\times[-h/2,h/2]$. Five different grids are used, from: $150\times50\times1$, up to, $2400\times800\times1$. These grids are henceforth denoted, respectively, by: $4h$, $2h$, h, $h/2$ and $h/4$. For velocity components, reduced temperature and density, Dirichlet boundary conditions are set at $x = 0$, $y = -1/2$ and $y = 1/2$. A Neumann boundary condition is used in the outlet $x = 2.0$. For the pressure, Neumann boundary conditions are applied at $x = 0$, $y = -1/2$ and $y = 1/2$. At the outlet a Dirichlet condition is retained. For all variables, periodicity is assumed in spanwise, (z), direction. Table 3 presents the values considered in this work for simulation of Eqs. (29)–(31).

The procedure of cycling some parts of the algorithm is used to enhance convergence and stability of the numerical scheme. Such procedure is based on the recent work of Shunn and Ham [47], but with some modifications. First a different equation of state is used, second a constraint on the divergence of the velocity field is added herein, as a part of the strategy retained to solve the Poisson problem. Finally, it is worth recalling that we are interested in density ratio values smaller than those considered in [47].

3.2.1. Unsteady error behavior

In this section we discuss the effects of the outer iterative procedure, i.e., the number of times that the balance, state and the Poisson equations are solved, before the numerical time integration scheme. The influence of the Courant number value on the evolution of the L_2 norm is also assessed.

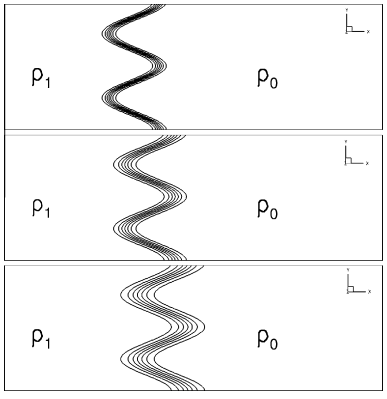

Fig. 3. Evolution of the density field. Top to bottom, $t = 0.0$, $t = 0.5$ and $t = 1.0$. From left to right, each isolines stands for an increase of 0.5 in density from $\rho_1 = 1$, until $\rho_0 = 5$.

Table 3
Values of the constant parameters for the variable density numerical simulation.

Parameter	Value	Parameter	Value
ρ_o	5	a	1/5
ρ_1	1	b	20
u_f	0.25	k_2	4π
v_f	0	ω	1
w_f	0	$\kappa = \mu$	10^{-4}
P_o	5	C_p	1

In order to quantify only the effects of spatial errors and cycling procedure in the analysis of order of accuracy of low Mach number MMS problems, a Courant number value is chosen, and then, the grid refinement procedure is performed and the subsequent analysis of order of accuracy is conducted.

Fig. 4 shows the unsteady evolution of the L_2 norm evaluated from the density field. In this case, the Courant number value for the simulations is set to 2. It is noteworthy that, specially for the refined grids, the increase in the number of cycles leads to a slight decrease in the magnitude of the L_2 norm and therefore an improvement in order of accuracy. It is also worth noting that such a behavior is also observed for the variables u, v and ϕ. In Fig. 5 the evolution of the L_2 norm of pressure is reported. Unlike the other primary variables of the system, as the number of cycles increases, the magnitude of the L_2 norm increases as well. However, it will be shown in the next section devoted to the analysis of order of accuracy for the low Mach number MMS that, even with such a negative sensitivity to the number of cycles, its order of accuracy is not penalized.

Although not shown here for the sake of conciseness, we have also found that the L_2 norm of primary variables errors smoothly decays with time as the front diffuses and the number of control volumes within the front increases. In fact, this is the reason that explains why the numerical simulations are stopped at $t = 1.0$.

Fig. 6 displays L_2 norm for different number of cycles for the h grid. The results clearly show that with higher values of Courant number, the use of more than five iterations in the cycling procedure does not provide any further gain in the reduction of error magnitude. However, for Courant number values up to unity, an increase in the number of cycles still gives rise to an improvement of the results.

3.2.2. Order of accuracy analysis

In this section we present and discuss the results of an order of accuracy analysis performed for the low Mach number MMS case. All the simulations presented below have been carried out with a constant value of the Courant number. Although the errors quantified herein by means of the L_2 norm is a rather complicated combination of both spatial and temporal approximations, performing the grid refinement with such a constant Courant number value allows to focus on the influence of the spatial discretization only, and this despite the presence of a residual temporal error since it will remains the same, provided that the Courant number value is kept constant.

Tables 4–6 display the order of accuracy, and the value of the L_2 norm obtained for velocity, density and reduced temperature for different numbers of cycles and a Courant number value Co = 2. These values of error and order of accuracy are measured at $t = 1.0$ [47].

Unlike the order of accuracy analysis conducted for the incompressible solution, where the values of the L_2 norm decrease with a constant order of accuracy, the present results show that, as the

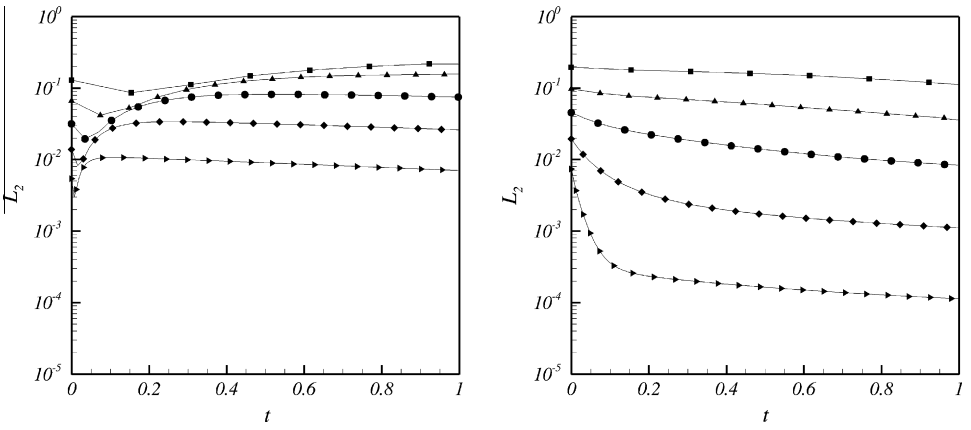

Fig. 4. Evolution in time of the L_2 norm for the density variable with 1 (left) and 10 (right) cycles. ■: $4h$, ▲: $2h$, ●: h, ♦: $h/2$, ►: $h/4$. For the sake of better visualization, the L_2 axis is in log scale.

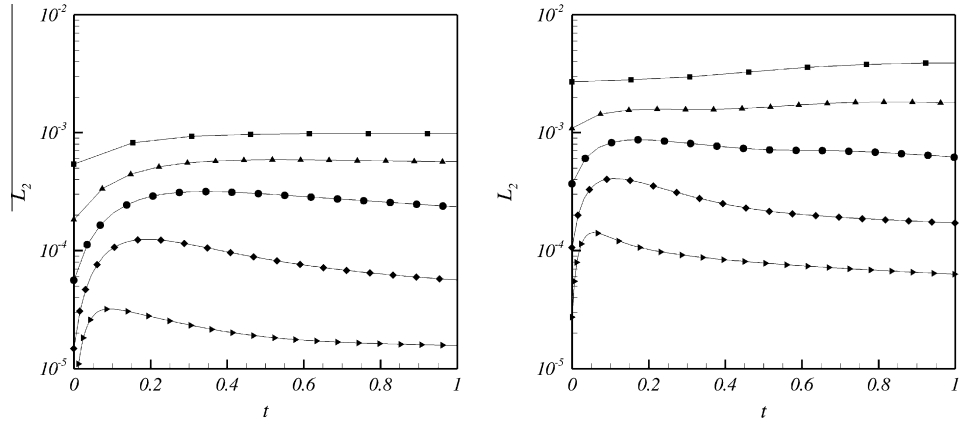

Fig. 5. Evolution in time of the L_2 norm for p with 1 (left) and 10 (right) cycles. ■: $4h$, ▲: $2h$, ●: h, ♦: $h/2$, ►: $h/4$. For the sake of better visualization, the L_2 axis is displayed in log scale.

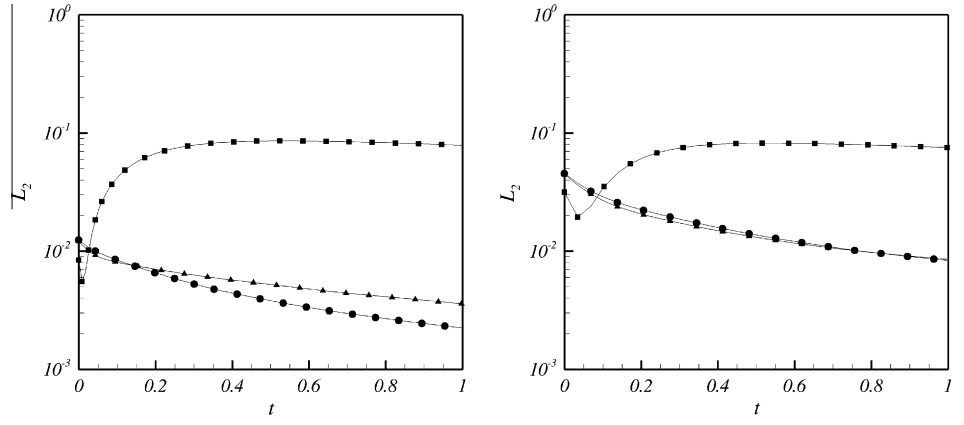

Fig. 6. Decay of the L_2 norm according to the number of cycles $CFL = 0.5$ (left) and $CFL = 2.0$ (right) for density. ■: Single cycle, ▲: 5 cycles, ●: 10 cycles. For the sake of better visualization, the L_2 axis is plotted in log scale.

grid is refined, not only the magnitude of the L_2 norm decreases, but also the order of accuracy increases. Such a trend is even more pronounced for velocity, density and reduced temperature when increasing the number of cycles. On the contrary, as far as the pressure field is concerned, the magnitude of the L_2 norm also increases for an increasing number of cycles.

Fig. 7 displays the order of accuracy achieved for both the pressure and the u-component of the velocity. The simulations are carried out using a constant value of the Courant number value Co = 2. From a careful examination of Tables 4–6, and Fig. 7, one can notice that the error decay is larger in single cycle simulations. A similar analysis (not reported) demonstrates that such a conclusion also holds for different Courant number values, and for all the primary variables.

The decays of the L_2 norm obtained for the primary variables, corresponding to the results gathered in Tables 4–6, are illustrated

Table 4
Order of accuracy for low Mach number solution, single cycle, Co = 2.

Domain	4h	q	2h	q	h	q	h/2	q	h/4	q
L_2u	8.82E−03	–	4.52E−03	0.96	1.65E−03	1.45	2.29E−04	2.85	1.91E−05	3.58
L_2v	3.06E−03	–	1.28E−03	1.25	3.27E−04	1.97	3.47E−05	3.24	3.44E−06	3.33
L_2p	9.82E−04	–	5.69E−04	0.79	2.44E−04	1.22	5.89E−05	2.05	1.59E−05	1.89
$L_2\phi$	1.03E−01	–	6.73E−02	0.61	2.39E−02	1.50	7.70E−02	1.01	1.40E−03	2.07
$L_2\rho$	2.18E−01	–	1.55E−01	0.49	7.70E−02	1.01	2.69E−02	1.52	7.31E−03	1.88

Table 5
Order of accuracy for low Mach number solution, five cycles, Co = 2.

Domain	4h	q	2h	q	h	q	h/2	q	h/4	q
L_2u	8.19E−03	–	2.50E−03	1.71	5.01E−04	2.32	7.55E−05	2.73	1.00E−05	2.92
L_2v	3.52E−03	–	1.17E−03	1.60	2.29E−04	2.35	2.82E−05	3.02	5.85E−06	2.27
L_2p	2.68E−03	–	1.24E−03	1.11	4.49E−04	1.47	1.36E−04	1.72	6.07E−05	1.17
$L_2\phi$	5.05E−02	–	1.16E−02	2.12	1.96E−03	2.57	2.98E−04	2.72	4.87E−05	2.61
$L_2\rho$	1.15E−01	–	3.83E−02	1.59	8.97E−03	2.09	1.32E−03	2.76	1.76E−04	2.91

Table 6
Order of accuracy for low Mach number solution, 10 cycles, Co = 2.

Domain	4h	q	2h	q	h	q	h/2	q	h/4	q
L_2u	8.50E−03	–	2.58E−03	1.72	4.52E−04	2.51	6.59E−05	2.78	9.73E−06	2.82
L_2v	3.14E−03	–	1.02E−03	1.63	2.05E−04	2.31	2.12E−05	3.27	4.24E−06	2.32
L_2p	3.90E−03	–	1.81E−03	1.11	6.44E−04	1.49	1.76E−04	1.87	6.49E−05	1.44
$L_2\phi$	4.19E−02	–	8.34E−03	2.33	1.26E−03	2.73	1.32E−04	3.25	1.29E−05	3.35
$L_2\rho$	1.21E−01	–	3.97E−02	1.61	5.55E−03	2.84	1.17E−03	2.24	1.19E−04	3.31

in Fig. 8. In this Figure, one can note a higher value of the order of accuracy as the number of cycles is increased. Even for the pressure, that is less sensitive to the number of cycles than the others variables, an increase in the order of accuracy is observed.

With regard to the effects of the number of cycles with respect to the order of accuracy, it is worth noticing that, as the grid mesh size is halved from h to $h/2$, and with a Courant number value Co = 2, the order of accuracy for the density is found to increase from 1.52 (Table 4, column 8, line 5) to 2.24 (Table 6, column 8, line 5), provided that the number of cycles is increased from 1 to 10.

4. Application of the numerical scheme to variable density scalar mixing layers

In the previous section, our focus has been placed only on code verification in terms of effective numerical precision with respect to theoretical order of accuracy, and this issue undoubtedly constitutes the central core of the present work. However, in a final section, we propose to shed some light on the stability and robustness of the present pressure-based finite volume scheme. It is worth emphasizing that the corresponding issues have not been addressed through the MMS analyses reported above. To avoid the possible onset of spurious short waves numerical instabilities, the computational simulations presented below have been conducted with the deferred correction approach to represent the advective terms [14]. It is worth noting that, with this numerical scheme, second order accuracy was also achieved from MMS verification. As already mentioned, the essential aim of the manufactured solutions described above is to allow for code verification, and it is mainly focused here on the evaluation of the order of accuracy. However, it is worth noting that the existence of singular discontinuities in the solutions, as well as the use of flux limiters or adaptive meshes, still constitute some among the crucial issues that remain with MMS applications [51–53].

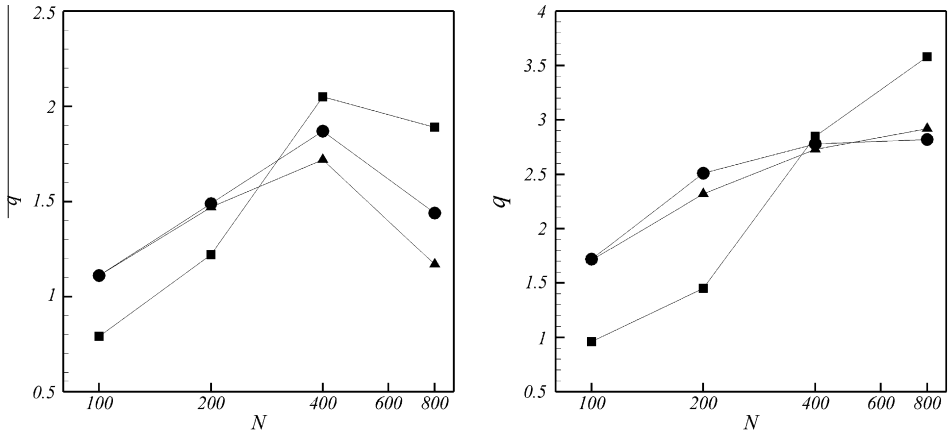

Fig. 7. Evolution of the order of accuracy q. Pressure (left), u (right). ■: Single cycle, ▲: 5 cycles, •: 10 cycles. For the sake of better visualization, the N axis is plotted in log scale.

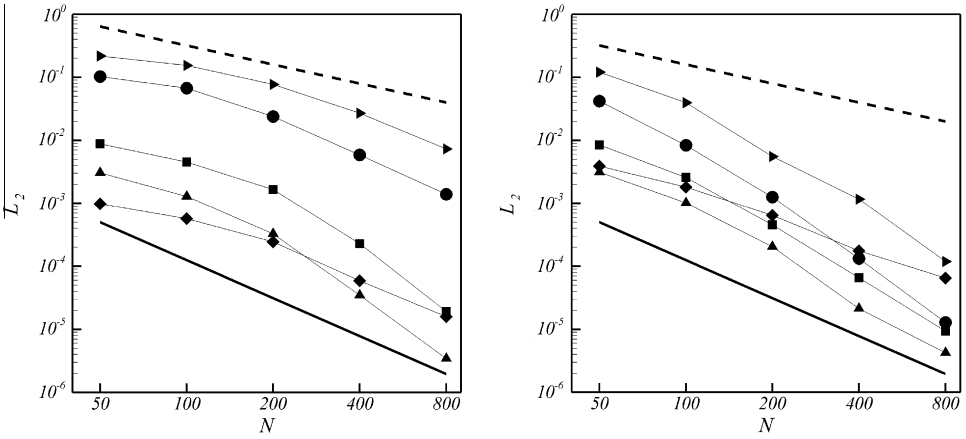

Fig. 8. Evolution in time of the L_2 norm. Single cycle (left), 10 cycles (right). ■: u, ▲: v, ♦: p, •: ϕ, ►:ρ. The solid line stands for the second order decay, and the dashed line stands for first order decay.

To proceed with the analysis of the robustness of the numerical scheme we investigate two classical problems associated with non reactive planar mixing layers between two inlet streams featuring different density values ρ_1 and ρ_2. Considering that the physical specificities of the corresponding flow fields have been already largely discussed in the literature, see for instance Ref. [54], our focus with these additional numerical simulations is not placed on the physical phenomenology itself but rather on the computational behavior and associated capabilities of the numerical scheme for different values of the characteristic density contrast defined as $1 - 1/s$ where $s = \rho_1/\rho_2 \geqslant 1$ denotes the density ratio between the two streams.

The first numerical configuration retained to perform this analysis corresponds to a two-dimensional temporally developing mixing layer involving transport of a passive scalar quantity ϕ and featuring increasing values of the density ratio $s = \rho_1/\rho_2$ where $\rho_1 = \rho(\phi_1)$ and $\rho_2 = \rho(\phi_2)$ denote the values of the density in the top and bottom streams, respectively.

The last test case is undoubtedly more representative of the difficulties that can be encountered when dealing with the numerical simulations of practical configurations. It corresponds to the Large Eddy Simulation of a spatially developing turbulent mixing layer [1,55,56]. In terms of both the density ratio $s = 3.3$, and Reynolds number $Re = 95{,}000$, these conditions are clearly more representative of those encountered in practical applications, such as the experimental results reported in Refs. [55,56].

4.1. Two-dimensional temporally developing mixing layers

This academic configuration appears as a well-suited test case to evaluate the response of the low Mach number solver scheme in terms of both efficiency and stability. The investigation is conducted for increasing values of the density contrast and, to maintain the resolution level compatible with a parametric analysis, two-dimensional numerical simulations are conducted for a moderate value of the Reynolds number. It is well-known that such two-dimensional calculations tend to overestimate the transverse velocity fluctuations statistics but, as mentioned above, we have here more interest in the response of the numerical scheme than in the ability of the simulations to fully recover all the details of the underlying physics. Finally, the issue associated with the consideration of higher values of the Reynolds number will be addressed in the last subsection of the manuscript.

The temporal mixing layer consists of two coflowing streams travelling in opposite directions with the same reference velocity $U_r = \Delta U/2$ where ΔU denotes the velocity difference across the layer. The flow variables reported below are normalized with respect to a reference length scale L_r equal to half the initial vorticity thickness, i.e., $L_r = \delta_\nu(t = 0)/2$. In the retained representation, x, and y denote the streamwise, and the cross-stream directions, respectively. The temporal mixing layers are initiated by a hyperbolic-tangent velocity profile, i.e., $u = U_r \tanh(y/L_r)$, with free stream conditions as $u_1 = U_r = 1$ and $\phi_1 = 1$ on the top, and $u_2 = -U_r = -1$ and $\phi_2 = 0$ on the bottom. A weak white noise random perturbation is superimposed on the initial velocity field in the rotational region. Periodic boundary conditions have been retained in the streamwise direction, and the longitudinal extent of the computational domain is defined according to Michalke's inviscid most unstable wavelength [54,57]. Slip conditions have been set in the transverse directions. Simulations are conducted for five different values of the density ratio $s = 1,2,4,6,8$ at $Re = 100$ where Re denotes the Reynolds number based on the reference velocity U_r and the initial vorticity thickness $\delta_\nu(t = 0)$. The computational mesh features homogeneous grid spacings $\Delta x = \Delta y = \Delta$, and two distinct resolution levels have been considered. In the first case, the number of grid points is set to $n_x = 2L_x/\Delta = 140$ in the longitudinal direction, and $n_y = 2L_y/\Delta = 140$ in the cross-stream direction, whereas the resolution has been doubled in the second set of numerical simulations, i.e., $n_x = n_y = 280$. Numerical simulations are conducted with a constant integration time step $\Delta t = 10^{-5}$ s. Once made non dimensional using the reference velocity U_r, and initial vorticity thickness $\delta_\nu(t = 0)$, it corresponds to $\Delta t^* = 0.0002$.

Fig. 9 displays simultaneously the scalar, pressure $P'(\mathbf{x})$, and normalized vorticity contours as obtained from the numerical simulations performed in cases $s = 1$ (case of reference) and $s = 2$. The results are made non dimensional using the reference velocity U_r, and initial vorticity thickness $\delta_\nu(t = 0)$, and they correspond to $t^* = 26.1$ and $t^* = 42.1$ for cases $s = 1$ and $s = 2$, respectively. The corresponding flowfield is dominated by the growth of large scale coherent structures of Kelvin–Helmholtz type. The non dimensional time t^* required to observe the birth of these coherent structures differs from one case with respect to another. The figure clearly evidences the ability of the numerical solver to recover the emergence of these two-dimensional structures.

Fig. 10 displays simultaneously the scalar and normalized vorticity fields obtained for increasing values of the density ratio from $s = 2$ up to $s = 8$. The results confirm that, in the present configuration, if the mixing layer development is controlled at leading order by the value of ΔU, it is also strongly influenced by the density ratio s, the baroclinic torque being one of the most well-known mechanisms that influences the corresponding flowfield dynamics [58].

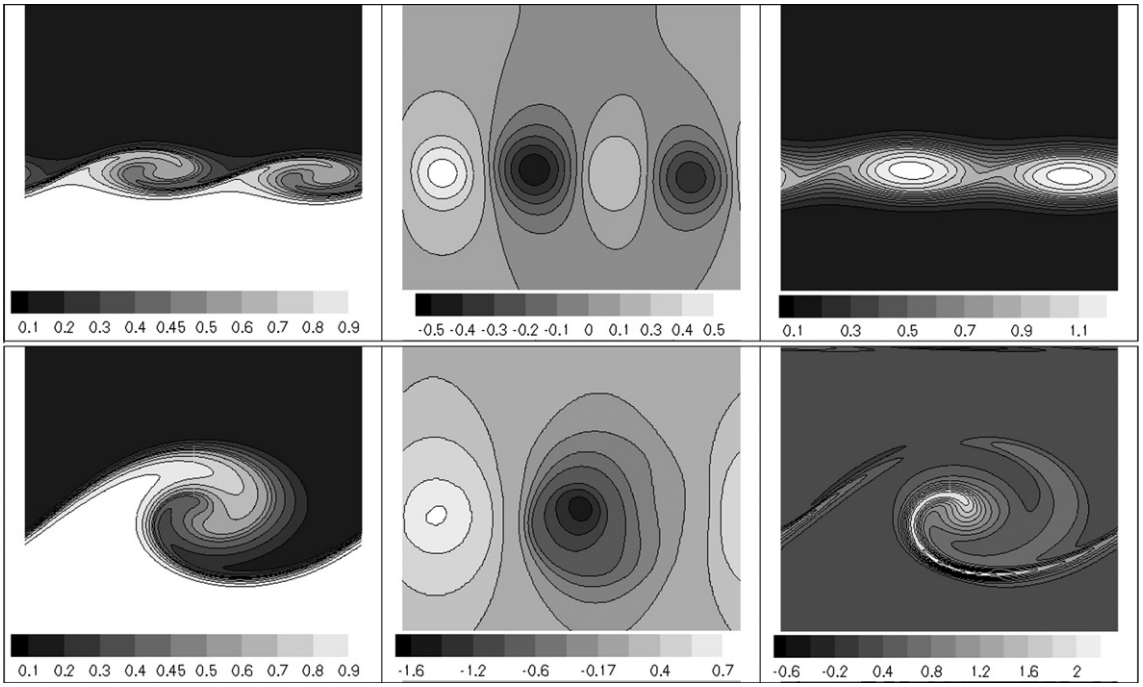

Fig. 9. From left to right: instantaneous snapshots of scalar, pressure $P'(\mathbf{x})$, and normalized vorticity contours as obtained from the numerical simulation of two-dimensional temporally developing mixing layers conducted at $s = 1$ at non dimensional time $t^* = 26.1$ (top) and $s = 2$ at non dimensional time $t^* = 42.1$ (bottom).

In Fig. 11, the temporal evolution of the Courant number is reported as a function of the non dimensional time t^*. For values of the density ratio $s = 1,2,4$, the variations of the Courant number, as defined by $Co = max\{\Delta t(2\mu_i/(\rho_i(\Delta x_i)^2) + (u_i/\Delta x_i))\}$ [14], remains bounded between the values $Co = 0$ and $Co = 0.25$. However, for higher values of the density ratio, i.e., $s = 6,8$, the figure clearly evidences the difficulties that are encountered by the numerical solver as the roll-up of vortices involving large density differences takes place.

Finally, in order to evaluate more quantitatively the response of the numerical scheme, some code performance parameters have been gathered in Table 7. It is worth noting that, whatever the case under consideration, convergence of the steps [3 and 4] of the proposed algorithm, see Table 2, is obtained in less than 3 iterations.

4.2. Three-dimensional spatially developing turbulent mixing layers

The present study is now finalized by considering a high speed turbulent mixing layer. The retained conditions are similar to those encountered in the early experimental analyses of turbulent premixed combustion conducted in Refs. [55,56]. In the corresponding experiments a premixed flow of methane and air is ignited, and stabilized thanks to a parallel flow of high temperature fully burned gases. The wind tunnel features a squared section with dimensions $800 \times 100 \times 100$ mm that is discretized into a finite volume computational mesh made up of $100 \times 50 \times 50$ control volumes in the directions x, y and z respectively. The inlet consists of two distinct ducts separated by a thin splitter plate. In the main (top) duct fresh reactants are injected, whereas high temperature combustion products are injected through the auxiliary (bottom) duct. No-slip boundary conditions are imposed at the boundary in both y and z directions. A convective boundary condition is set at the outlet of the computational domain.

The mean velocity profile at inlet is imposed using a hyperbolic function:

$$\bar{u}(z) = \frac{\bar{u}_q - \bar{u}_p}{2} + \frac{\bar{u}_q + \bar{u}_p}{2} \tanh\left(\frac{2h(z)}{\delta_m} - \frac{2h_p}{\delta_m}\right), \tag{35}$$

where $\bar{u}_q$ and $\bar{u}_p$ denote the mean velocity values in the auxiliary burner and main duct, respectively, h_p is the height of auxiliary duct, and δ_m is the prescribed width of the mixing layer. The main duct incoming flow is characterized by a maximum longitudinal velocity $\bar{u}_p = 65$ m/s whereas the auxiliary duct incoming flow features a maximum longitudinal velocity $\bar{u}_q = 130$ m/s. The Reynolds number Re, based on the main duct incoming flow velocity, its height, and the value of the kinematic viscosity of air at 600 K is of the order of $Re \approx 95{,}000$. The resolution required to deal with such a high Reynolds number turbulent flow is impracticable for a direct numerical simulation of the Navier–Stokes equations, and we resort to the LES filtered set of Navier–Stokes equations. The classical Smagorinsky closure is retained to represent the influence of unresolved subgrid-scale fluctuations effects [59]. The Smagorinsky constant value is set to $C_S = 0.18$, and the closure is used in conjunction with the Van-Driest damping function [14]. It is outside the scope of the present study to report the details of turbulent combustion modelling in such conditions. Therefore, only non reactive flow fields featuring either the same density ratio as the one encountered in the experiments, i.e., $s = 3.3$, or no density fluctuations, i.e., $s = 1$ (case of reference) are considered below.

For the present Large Eddy Simulations, a methodology based on the use of digital filters has been retained to generate realistic fluctuating inlet boundary conditions [60]. Such an approach requires to generate an entire set of random number data which can then be processed using digital filters in such a manner that the resulting set of filtered data will present desired statistical properties such as spatial and temporal correlations [60]. An interesting feature of this approach is its ability to recover anisotropic turbulence properties which is of crucial importance to perform Large Eddy Simulations of practical applications such as the one considered here.

Instantaneous snapshots obtained from the three dimensional simulations of the flow described above are reported in Figs. 12 and 13. The property Q offers an interesting way to evidence the flow field coherent structures [61]. For a flow of uniform density, the corresponding quantity, i.e., the second invariant Q of the velocity-gradient tensor $\partial u_i/\partial x_j$, is related to the Laplacian of the

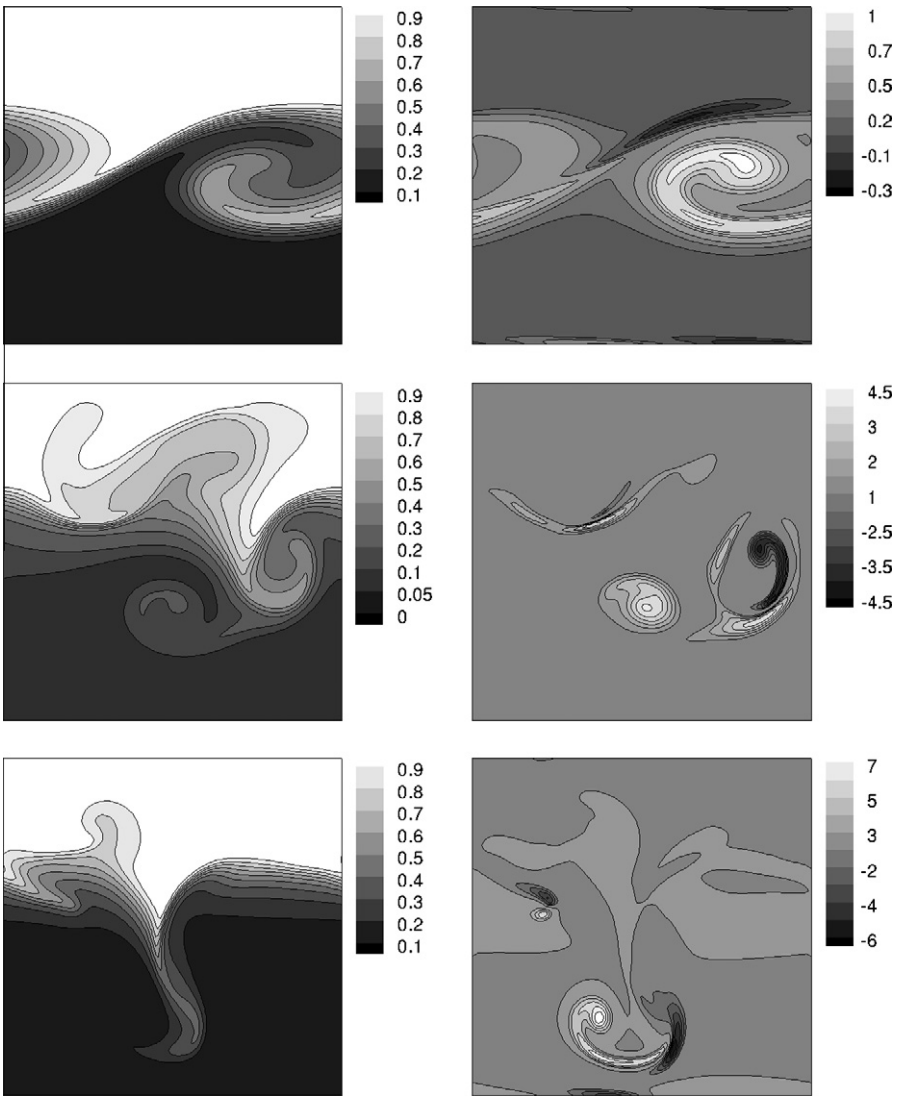

Fig. 10. From top to bottom: instantaneous snapshots obtained for increasing values of the density ratio, $s = 2$ (top), $s = 4$ (middle), $s = 8$ (bottom); on the right: scalar field; on the left: vorticity contours.

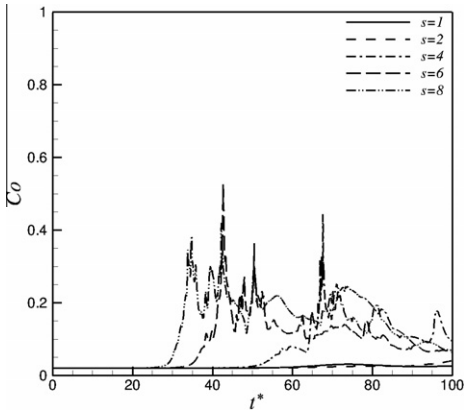

Fig. 11. Temporal evolution of the Courant number *Co* for different values of the density ratio.

pressure field, and positive iso-values of Q are often used to characterize low pressure tubes that are generally associated with coherent structures. In Figs. 12 and 13 the isosurface of the property $Q = 2^6$ have been displayed. The high value retained in this case results from the fact that the flow is a high velocity, high Reynolds number, confined flow. In Fig. 12, Kelvin–Helmholtz structures that are characteristic of the mixing layers dynamics can be recognized downstream of the computational domain inlet. In comparison with the case of reference, i.e., $s = 1$, the isosurface reported in Fig. 13 features smaller characteristic length scales. The two figures also evidence the strong three-dimensionality of the flow which results, to a large extent, from the fluctuating boundary conditions that have been used at the inlet of the computational domain.

Table 7
Code performance parameters for different density ratios; grid 140^2. *Note*: in the first column [3,4] denote two steps of the algorithm described previously in Table 1.

	$s = 1$	$s = 2$	$s = 4$	$s = 6$	$s = 8$
CPU time (s)	3865	4484	4576	4496	4607
Iteration Nb. (step [3])	3	3	3	3	3
Iteration Nb. (step [4])	1	1	2	2	2
Co (max. value)	0.030	0.040	0.443	0.526	0.419
Co ($t^* = 100$)	0.025	0.040	0.092	0.064	0.069
Co (average value)	0.023	0.023	0.077	0.088	0.123

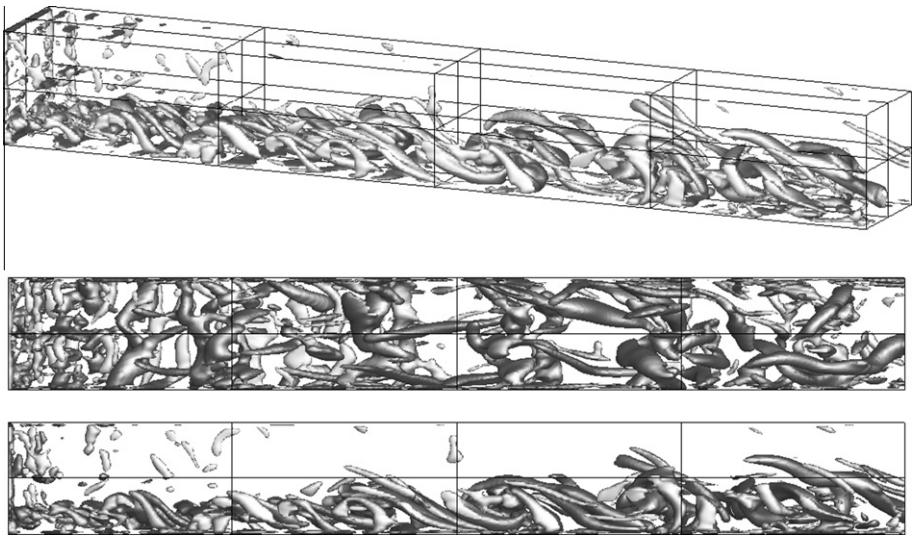

Fig. 12. Perspective, top and lateral views of the iso-value surface of the second invariant of the velocity-gradient tensor $Q = 2^6$, at $t = 0.020$ s. The density ratio is set to $s = 1$.

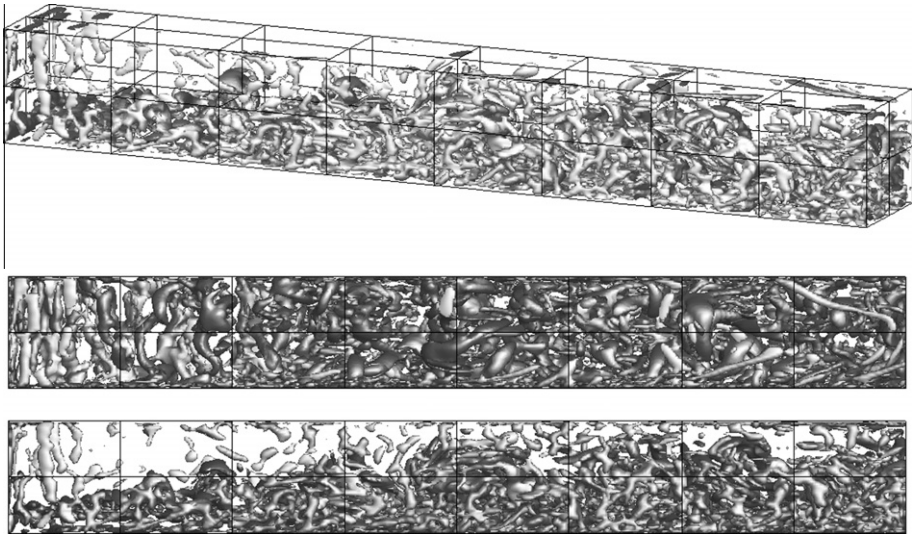

Fig. 13. Perspective, top and lateral views of the iso-value surface of the second invariant of the velocity-gradient tensor $Q = 2^6$, at $t = 0.020$ s. The density ratio is set to $s = 3.3$.

Finally, longitudinal slices of the normalized temperature field as obtained from the numerical simulations conducted with uniform density field, i.e., $s = 1$, or with a density contrast that is representative of the experimental reactive conditions, i.e., $s = 3.3$, have been reported in Fig. 14.

Together with the previous verification of the discretization scheme performed thanks to MMS, the results discussed above provide some interesting insights on the stability and robustness of the numerical solver. As suggested by one of the reviewers of the manuscript, it would have been also interesting to evaluate the computational efficiency of the present numerical scheme through a detailed comparison with others simulations performed using higher order, multigrid or adaptive methods. However, such an analysis definitely exceeds the scope of the present study. Finally, it is worth emphasizing that the MMS verification step undoubtedly facilitates the subsequent application of the solver to more complex situations. This confirms that even if MMS are applied to smooth and simple problems, it does serves, and should be used, as a well-suited preliminary test before coping with other problems that are physically more demanding.

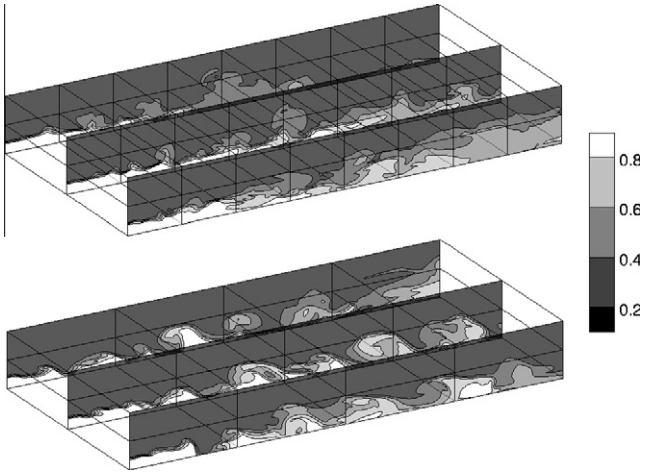

Fig. 14. Longitudinal slices of the normalized temperature field as obtained from the numerical simulations conducted with uniform density field, i.e., $s = 1$ (top of the figure), or with a density contrast that is representative of the experimental reactive conditions, i.e., $s = 3.3$ (bottom of the figure).

5. Conclusions

We have described a procedure for code verification (i) to determine whether, or not, a numerical code solves its governing equations correctly, and (ii) to preview how such a numerical scheme behaves when dealing with real problems. The numerical procedure relies on the manufacture of a general solution of the system of governing equations. Generality of the solution is essential because it guarantees that few, if any, code capabilities will remain unverified.

Two MMS problems are considered. First, a fully incompressible manufactured solution is proposed, achieving the expected order of accuracy. Second, an analytical propagating front separating heavy from light gases is considered. A variable coefficient Poisson solver is used to simulate the corresponding low Mach number flow. A physically consistent constraint is used to ensure that the velocity field is solved correctly. Such a combination of the velocity constraint and the variable-coefficient Poisson solver is found of fundamental importance to ensure both the numerical stability and the expected order of accuracy. An inner iteration procedure is implemented, and despite its high numerical cost, the improvements in terms of both the order of accuracy and error magnitude are undeniable. In this respect, further investigations may be carried out since although possible, the order of accuracy q does not always converge monotonically.

The present results also suggest that determining the optimal operating conditions in terms of grid size, Courant number value, number of outer iterations, etc. is a nontrivial and problem-dependent task that deserves more attention than currently afforded.

Although not fully physically consistent – since the MMS is more a mathematical exercise rather than a real attempt of reproducing a real life experiment or physical problem – the procedure of verification allows to gain more insights into the capabilities and limitations of the numerical code we presented to deal with variable density flow fields representative of those encountered in situations relevant of combustion. It is completed herein by a brief stability and robustness illustration of the pressure-based finite-volume numerical scheme. Very encouraging results have been obtained, and the numerical scheme appears as a good candidate for further studies devoted to Large Eddy Simulation of turbulent combustion.

Acknowledgments

This work was performed while L.F. Figueira da Silva was on leave from Centre National de la Recherche Scientifique, Poitiers (France). The authors would like to thank CNPq, FAPEMIG and PETROBRAS S.A. for the financial support.

References

[1] Andrade FO, Figueira da Silva LF, Mura A. Large eddy simulation of turbulent premixed combustion at moderate Damköhler numbers stabilized in a high speed flow. Combust Sci Technol 2011;183:645–64.
[2] Mura A, Demoulin FX. Lagrangian intermittent modeling of turbulent lifted flames. Combust Theory Model 2007;11(2):227–57.
[3] Robin V, Mura A, Champion M, Degardin O, Renou B, Boukhalfa M. Experimental and numerical analysis of stratified turbulent V-shaped flames. Combust Flame 2008;153:288–315.
[4] Mura A, Champion M. Relevance of the Bray number in the small-scale modeling of turbulent premixed flames. Combust Flame 2009;156:729–33.
[5] Oberkampf WL, Trucano TG. Verification and validation in computational fluid dynamics. Rev Article Prog Aero Sci 2002;38(3):209–72.
[6] Eça L, Hoekstra M. Evaluation of numerical error estimation based on grid refinement studies with the method of the manufactured solutions. Comput Fluids 2009;38:1580–91.
[7] Anderson JD. Computational fluids dynamics: the basics with applications. Mac Graw-Hill Ed; 1995.
[8] Figueira da Silva LF, Azevedo JLF, Korzenowski H. Unstructured adaptive grid flow simulations of inert and reactive gas mixtures. J Comput Phys 2000;160:522–40.
[9] Turkel E, Radespiel R, Kroll N. Assessment of preconditioning methods for multidimensional aerodynamics. Comput Fluids 1997;26(6):613–34.
[10] Roller S, Munz C. A low Mach number scheme based on multi-scale asymptotics. Comput Visual Sci 2000;3(1–2):85–91.
[11] Choi YH, Merkle CL. The application of preconditioning in viscous flows. J Comput Phys 1993;105:207–23.
[12] Turkel E. Review of preconditioning methods for fluid dynamics. Appl Numer Math 1993;12:257–84.
[13] Darmofal DL, Schmid PJ. The importance of eigenvectors for local preconditioners of the euler equations. J Comput Phys 1996;127(2):346–62.
[14] Ferziger J, Peric M. Computational methods for fluid dynamics. 3rd ed. New York: Springer-Verlag; 2002.
[15] Dourado WMC, Bruel P, Azevedo JLF. A time-accurate pseudo-compressibility approach based on a unstructured hybrid finite volume technique applied to unsteady turbulent premixed flame propagation. Int J Numer Met Fluids 2004;44:1063–91.
[16] Ramshaw JD, O'Rourke PJ, Stein LR. Pressure gradient scaling method for fluid flow with nearly uniform pressure. J Comput Phys 1985;58(3):361–76.
[17] Amsden AA, O'Rourke PJ, Butler TD. KIVA-II A computer program for chemically reactive flows with sprays. KIVA II manual, LA-11560-MS. Los Alamos National labotarories; 1989.
[18] Wang Y, Trouvé A. Artificial acoustic stiffness reduction in fully compressible, direct numerical simulation of combustion. Combust Theory Model 2004;8(3):633–60.
[19] Papageorgakis GC, Assanis DN. Comparison of linear and non-linear RNG-based K-ε models for incompressible turbulent flows. Num Heat Transfer, Part B 1999;35(1):22.
[20] Chorin AJ. Numerical solution of the Navier–Stokes equations. Math Comput 1968;22:745–62.
[21] Lima e Silva ALF, Silveira-Neto A, Damasceno JJR. Numerical simulation of two dimensional flows over a circular cylinder using the immersed boundary method. J Comput Phys 2003;189:351–3706.
[22] Chorin AJ, Marsden JE. A mathematical introduction to fluid mechanics. 3rd ed. New York: Springer-Verlag; 1993.
[23] Patankar SV. Numerical heat transfer and fluid Flow. 3rd ed. New York: McGraw-Hill; 1980.
[24] Najm HN, Wyckoff PS, Knio OM. A semi-implicit numerical scheme for reacting flows. J Comput Phys 1998;143:381–402.
[25] Cook AW, Riley JJ. Direct numerical simulation of a turbulent reactive plume on a parallel computer. J Comput Phys 1996;129:263–83.
[26] Rauowens P, Vierendeels J, Merci B. A Solution for the odd–even decoupling problem in pressure-correction algorithms for variable density flows. J Comput Phys 2007;227:79–99.
[27] Colella P, Pao K. A projection method for low speed flows. J Comput Phys 1999;149:245–69.
[28] Karki KC, Patankar SV. Pressure based calculation procedure for viscous flows at all speed in arbitrary configurations. AIAA J 1989;27(9):1167–74.
[29] Bell JB. AMR for low Mach number reacting flows. LBNL Report LBNL-54351. In: Proceedings of the Chicago workshop on adaptive mesh refinement methods; 2003.
[30] Lessani B, Papalexandris MV. Time-accurate calculation of variable density flows with strong temperature gradients and combustion. J Comput Phys 2006;212(1):218–46.
[31] Knio OM, Najm HN, Wyckoff PS. A Semi-implicit numerical scheme for reacting flow: II. Stiff, operator-split formulation. J Comput Phys 1999;154(2):428–67.
[32] Rider WJ, Kothe DB, Puckett EG, Aleinov ID. Accurate and robust methods for variable density incompressible flows with discontinuities. In: Barriers and challenges in computational fluid dynamics. Boston: Kluwer Academic Publishers; 1998. p. 213–30.
[33] Steinberg S, Roache PJ. Symbolic manipulation and computational fluid dynamics. J Comput Phys 1985;57(2):251–84.
[34] Roache PJ, Knupp P, Steinberg S, Blaine RL. Experience with benchmark test cases for groundwater flow. In: Celik I, Freitas CJ, editors. ASME FED, vol. 93. Benchmark test cases for computational fluid dynamics; 1990. p. 49–56 [Book No. H00598-1990].
[35] Roache PJ. Verification of codes and calculations. AIAA J 1998;36:696–702.
[36] Salari K, Knupp P. Code verification by the method of manufactured solutions. Sandia report, SAND2000-1444. Sandia National Laboratories; 2000.
[37] Ceniceros HD, Roma AM. A nonstiff, adaptive mesh refinement-based method for the Cahn–Hilliard equation. J Comput Phys 2007;255(2):1849–62.
[38] Ascher UM, Ruuth SJ, Wetton BTR. Implicit–explicit methods for time-dependent partial differential equations. SIAM J Numer Anal 1995;32(3):797–823.
[39] Nicoud F. Conservative high-order finite-difference schemes for low Mach number flows. J Comput Phys 2000;255(2):1849–62.
[40] Rhie CM, Chow WL. Numerical study of the turbulent flow past an airfoil with trailing edge separation. AIAA J 1983;21:1525.
[41] Shen WZ, Michelsen JA, Sorensen NN, Sorensen JN. An improved SIMPLEC method on collocated grids for steady and unsteady flow computations. Numer Heat Transfer, Part B 2003;43:221–39.
[42] Versteeg HK, Malalasekera W. An introduction to computational fluid dynamics. Ed. Prentice Hall; 1995.

[43] Harlow FH, Welsh JE. Numerical calculation of time dependent viscous incompressible flow with free surface. Phys Fluids 1965;8:2182–9.
[44] Jameson A, Schmidt W, Turkel E. Numerical solution of the Euler equations by finite volume methods using RungeKutta time stepping schemes. In: AIAA fluid and plasma dynamics conference; 1981. 15pp.
[45] Bogey C, Bailly C. A family of low dispersive and low dissipative explicit schemes for flow and noise computations. J Comput Phys 2004;194: 194–214.
[46] Schneider GE, Zedan M. A Modified strongly implicit procedure for the numerical solution of field problems. Numer Heat Transfer 1981;4:1–19.
[47] Shunn L, Ham F. Method of manufactured solutions applied to variable-density flows solvers. Ann Res Briefs – Center Turbul Res 2007:155–68.
[48] Shunn L, Knupp P. Verification of the low-mach number combustion codes using the method of manufactured solutions. CSRI Summer Proc – Sandia Natl Lab 2007:126–36.
[49] Nos RL. Simulacões de escoamentos tridimensionais bifásicos empregando métodos adaptativos e modelos de campo de fase, PhD thesis. Universidade de Sao paulo, Sao Paulo, SP, Brasil; 2007.
[50] Ceniceros HD, Nós RL, Roma AM. Three-dimensional, fully adaptive simulations of phase-field fluid models. J Comput Phys 2010;229(17):6135–55.
[51] Roache PJ. Fundamentals of verification and validation. New Mexico: Hermosa Publishers; 2009.
[52] Eça L, Hoekstra M, Hay A, Pelletier D. On the construction of manufactured solutions for one and two-equation eddy-viscosity models. Int J Numer Met Fluids 2007;54(2):119154.
[53] Eça L, Hoekstra M, Hay A, Pelletier D. A manufactured solution for a two-dimensional steady wall-bounded incompressible turbulent flow. Int J Comput Fluid Dyn 2007;21(3–4):175–88.
[54] Comte P, Lesieur M, Lamballais E. Large and small-scale stirring of vorticity and a passive scalar in a 3-D temporal mixing layer. Phys Fluids A 1992;4(12):2761–78.
[55] Moreau P, Boutier A. Laser velocimeter measurements in a turbulent flame. Symp (Int) Combust 1977;16:1747–56.
[56] Magre P, Moreau P, Collin G, Borghi R, Péalat M. Further studies by CARS of premixed turbulent combustion in a high velocity flow. Combust Flame 1988;71:147–68.
[57] Michalke A. On the inviscid instability of the hyperbolic tangent velocity profile. J Fluid Mech 1964;19:543–56.
[58] Lesieur M. Turbulence in fluids. 3rd revised and enlarged ed. Dordrecht: Kluwer Academic Publishers; 1997.
[59] Smagorinsky J. General circulation experiments with primitive equations. Mon Weather Rev 1963;91:99–164.
[60] Klein M, Sadiki A, Janika J. A digital filter based generation of inflow data for spatially developing direct numerical or large eddy simulations. J Comput Phys 2003;186:652–65.
[61] Jeong J, Hussain F. On the identification of a vortex. J Fluid Mech 1995;285:69–94.